IJMMM International Journal of Minerals, Metallurgy and Materials 矿物冶金与材料学报（英文版）

Synthesis, characterization and radioluminescence properties of erbium-doped yttria phosphors

Fatma Unal, Faruk Kaya, and Kursat Kazmanli

Cite this article as:
Fatma Unal, Faruk Kaya, and Kursat Kazmanli, Synthesis, characterization and radioluminescence properties of erbium-doped yttria phosphors, *Int. J. Miner. Metall. Mater.*, 28(2021), No. 12, pp. 1983-1990. https://doi.org/10.1007/s12613-021-2269-3

View the article online at SpringerLink or IJMMM Webpage.

Articles you may be interested in

Zhang-lin Chen, Kai Liu, Xuan-yi Yuan, and Ke-xin Chen, Luminescence properties of nitrogen-rich Ca-SiAlON:Eu^{2+} phosphors prepared by freeze-drying assisted combustion synthesis, *Int. J. Miner. Metall. Mater.*, 27(2020), No. 5, pp. 687-692. https://doi.org/10.1007/s12613-019-1934-2

Li-ping Wang, Fu Zhang, Shuai Chen, and Zi-heng Bai, One-pot synthesis and optical properties of In-and Sn-doped ZnO nanoparticles, *Int. J. Miner. Metall. Mater.*, 24(2017), No. 4, pp. 455-461. https://doi.org/10.1007/s12613-017-1426-1

Saeid Mersagh Dezfuli, Ali Shanaghi, and Saeid Baghshahi, Effect of Al_2O_3 and Y_2O_3 on the corrosion behavior of ZrO_2-benzotriazole nanostructured coatings applied on AA2024 via a sol-gel method, *Int. J. Miner. Metall. Mater.*, 25(2018), No. 11, pp. 1344-1353. https://doi.org/10.1007/s12613-018-1688-2

Faramarz Kazemi, Farzin Arianpour, Mahdiar Taheri, Ali Saberi, and Hamid Reza Rezaie, Effects of chelating agents on the sol–gel synthesis of nano-zirconia: Comparison of the Pechini and sugar-based methods, *Int. J. Miner. Metall. Mater.*, 27(2020), No. 5, pp. 693-702. https://doi.org/10.1007/s12613-019-1933-3

Tian-xing Lu, Cun-guang Chen, Zhi-meng Guo, Pei Li, and Ming-xing Guo, Tungsten nanoparticle-strengthened copper composite prepared by a sol-gel method and *in-situ* reaction, *Int. J. Miner. Metall. Mater.*, 26(2019), No. 11, pp. 1477-1484. https://doi.org/10.1007/s12613-019-1889-3

Hai-tao Wang, Zi-xiang Wang, Lian-zheng Wang, Jing-qin Wang, and Yan-cai Zhu, Effect of sintering temperature on the physical properties and electrical contact properties of doped $AgSnO_2$ contact materials, *Int. J. Miner. Metall. Mater.*, 25(2018), No. 11, pp. 1275-1285. https://doi.org/10.1007/s12613-018-1680-x

IJMMM WeChat

QQ author group

International Journal of Minerals, Metallurgy and Materials
Volume 28, Number 12, December 2021, Page 1983
https://doi.org/10.1007/s12613-021-2269-3

Synthesis, characterization and radioluminescence properties of erbium-doped yttria phosphors

Fatma Unal[1)], *Faruk Kaya*[2)], *and Kursat Kazmanli*[2)]

1) Metallurgical and Materials Engineering Department, Hitit University, Corum 19030, Turkey
2) Metallurgical and Materials Engineering Department, Istanbul Technical University, Maslak, Istanbul 34469, Turkey
(Received: 14 December 2020; revised: 18 February 2021; accepted: 21 February 2021)

Abstract: Radioluminescence (RL) behaviour of erbium-doped yttria nanoparticles (Y_2O_3:Er^{3+} NPs) which were produced by sol–gel method was reported for future scintillator applications. NPs with dopant rates of 1at%, 5at%, 10at% and 20at% Er were produced and calcined at 800°C, and effect of increased calcination temperature (1100°C) on the RL behaviour was also reported. X-ray diffraction (XRD) results showed that all phosphors had the cubic Y_2O_3 bixbyite-type structure. The lattice parameters, crystallite sizes (CS), and lattice strain values were calculated by Cohen-Wagner (C-W) and Williamson-Hall (W-H) methods, respectively. Additionally, the optimum solubility value of the Er^{3+} dopant ion in the Y_2O_3 host lattice was calculated to be approximately 4at% according to Vegard's law, which was experimentally obtained from the 5at% Er^{3+} ion containing solution. Both peak shifts in XRD patterns and X-ray photoelectron spectroscopy (XPS) analyses confirmed that Er^{3+} dopant ions were successfully incorporated into the Y_2O_3 host structure. High-resolution transmission electron microscopy (HRTEM) results verified the average CS values and agglomerated NPs morphologies were revealed. Scanning electron microscopy (SEM) results showed the neck formation between the particles due to increased calcination temperature. As a result of the RL measurements under a Cu K_α X-ray radiation (wavelength, λ = 0.154 nm) source with 50 kV and 10 mA beam current, it was determined that the highest RL emission belonged to 5at% Er doped sample. In the RL emission spectrum, the emission peaks were observed in the wavelength ranges of 510–575 nm ($^2H_{11/2}$, $^4S_{3/2}$–$^4I_{15/2}$; green emission) and 645–690 nm ($^4F_{9/2}$–$^4I_{15/2}$; red emission). The emission peaks at 581, 583, 587, 593, 601, 611 and 632 nm wavelengths were also detected. It was found that both dopant rate and calcination temperature affected the RL emission intensity. The color shifted from red to green with increasing calcination temperature which was attributed to the increased crystallinity and reduced crystal defects.

Keywords: sol–gel; erbium-doped yttria phosphors; microstructural parameters; X-ray excitation; radioluminescence emission

1. Introduction

Phosphors convert different types of excitation energy such as light, electricity, heat, X-ray, acoustic wave to visible light, depending on their composition. The phosphors are mainly composed of a host crystal and a small amount of activator(s) or dopant [1–5]. Oxide host materials have attracted great interest as they have higher corrosion resistance, high thermal stability, and low toxicity compared to the sulphides, which render them environmentally friendly host materials [3,6]. There are many oxide host materials such as Y_2O_3, Lu_2O_3, Sc_2O_3, La_2O_3, In_2O_3, Gd_2O_3, and yttria-stabilized zirconia (YSZ) [7–14]. Among these, Y_2O_3 is an important host material for Er dopant element because of similarities between Y^{3+} and Er^{3+} in ionic radii as well as the same crystal structures of Er_2O_3 and Y_2O_3 [7,15]. Additionally, it has broad transmittance (230–8000 nm), high melting point (2400°C), high refractive index (1.91), low phonon energy (380 cm^{-1}), large band gap (5.8 eV), and high chemical stability [1,7,16–17]. Er doped Y_2O_3 (Y_2O_3:Er^{3+}) powders can be produced by a large variety of methods such as sol–gel method [1], solvothermal [16], combustion technique [17], hydrothermal method [18], emulsion liquid membrane system [19], laser ablation [20], and spray pyrolysis [21]. They have many application areas such as optical sensors [17], infrared to visible light converters [19], temperature-sensing thermometry [22], biolabeling [23], solar cells [24], optical heaters [25], lasers [26], and scintillators [27]. In addition to the ionic radius similarities with rare earth ions, Y_2O_3 has very good radiation stability and is one of the most preferred sesquioxide hosts for scintillator applications [28–29]. Scintillators can be defined as phosphorus materials that allow the

Corresponding author: Fatma Unal E-mail: fatmaunal@hitit.edu.tr

conversion of high energy ionizing radiation (e.g., X-rays) into visible or UV light. The scintillators appear in many areas such as medical imaging systems (X-ray radiography, fluoroscopy, computed tomography gamma camera, positron emission tomography), security control, well-logging, high-energy physics, and astrophysics [30–33]. While the publications examining the cathodoluminescence (electrons as excitation source) properties of Er-doped Y_2O_3 scintillator powders are limited [34–36], there is only one study reported on the radioluminescence (RL, X-rays as excitation source) properties [37]. Avram *et al.* [37] investigated the RL behavior of 1at% Er doped Y_2O_3 nanoparticles (NPs) under Mo K_α X-ray excitation. They also studied the effect of Li co-doping and calcination temperature (1100°C) on the RL emission intensity. Even though, their up-conversion emission intensities under 1533 nm excitation reportedly increased with dopant rate, they indicated a decrease on RL emission intensity. However, there is no comprehensive result on the relation of dopant rate/microstructural parameters and RL emission of Er doped Y_2O_3 NPs. Therefore, herein, we report the first study on the effects of dopant rate, calcination temperature, and microstructural parameters on the RL emission behavior of Y_2O_3:Er^{3+} nanophosphors produced by facile sol–gel method.

2. Experimental

2.1. Synthesis of Y_2O_3:Er^{3+} phosphors

The phosphors were produced by sol–gel method using analytical grade, 99.99% purity, yttrium–nitrate–hexahydrate ($Y(NO_3)_3{\cdot}6H_2O$), erbium–nitrate–pentahydrate ($Er(NO_3)_3{\cdot}5H_2O$), and citric acid as the starting materials. The required amounts of $Y(NO_3)_3{\cdot}6H_2O$ and $Er(NO_3)_3{\cdot}5H_2O$ nitrate salts were dissolved in deionized water to produce 1at%, 5at%, 10at%, and 20at% Er doped Y_2O_3 phosphor powders. After the dissolution, 8 mL of citric acid ($C_6H_8O_7$) was added to 300 mL of solutions as the chelating agent. The pH value was adjusted to approximately 1 for all solutions, and NH_4OH was gradually added to adjust the pH values to 7. The solutions were stirred in a magnetic stirrer for 2 h. The filtered gels were dried at 85°C for 12 h. The dried powders were calcined at 800 and 1100°C for 3 h in a muffle furnace. The sample designations and synthesis parameters were given in Table 1.

2.2. Characterization studies

Differential thermal analysis (DTA) and thermogravimetric analysis (TG) were conducted at a rate of 10°C/min in order to determine the calcination temperatures of Er-doped powders. The crystal structure and microstructural parameters of the calcined samples were evaluated by means of X-ray diffraction technique (XRD) using Philips PW3710 X'Pert Pro. A monochromatic Cu K_α radiation was used for the XRD analysis. The measurements were performed between 10° and 90°, 2θ diffraction angles with 0.02° step size and 1 step/min scan rate parameters. The lattice parameters (LP) were calculated from the XRD patterns by means of Cohen-Wagner (C-W) method [1]. Furthermore, average crystallite size (CS) values of the powders were calculated utilizing the full width at half maximum (FWHM) values of the XRD peaks by means of Williamson-Hall (W-H) method [1]. In order to determine the instrumental broadening a Si calibration sample was used. The line broadening of the diffraction peaks (β_{hkl}) was calculated by Eq. (1),

$$\beta_{hkl} = [(\beta_{hkl})^2_{\text{measured}} - (\beta)^2_{\text{instrumental}}]^{1/2} \quad (1)$$

the average crystallite sizes of the powders were calculated by the following Williamson-Hall Eq. (2),

$$\beta_{hkl}\cos\theta = \frac{k\lambda}{D} + 4\varepsilon\sin\theta \quad (2)$$

where k is a constant (0.89), λ is the wavelength of the X-ray source (0.154 nm), D is average crystallite size, $(\beta_{hkl})_{\text{measured}}$ is measured broadening of hkl diffraction peaks, $(\beta)_{\text{instrumental}}$ is corrected instrumental broadening, and ε is the lattice strain. The dislocation density values, as a magnitude for crystal defects, were obtained from the calculated CS values by applying Williamson-Smallman relation [38] (Eq. (3)):

$$\delta = \frac{1}{D^2} \quad (3)$$

where D is crystallite size (nm) and δ is dislocation density (nm^{-2}). The doping levels were examined according to Vegard's law [39], as given in Eq. (4),

$$a_{\text{phosphor}} = (1-x)\,a_{Er_2O_3} + x a_{Y_2O_3} \quad (4)$$

where a_{phosphor} is the lattice parameter of the Er doped yttria powders; $a_{Er_2O_3}$ and $a_{Y_2O_3}$ are the lattice parameters of the pure Er_2O_3 and Y_2O_3 oxides having Ia-3 crystal structure; x is the mole fraction of Y_2O_3. The lattice parameter value of un-doped Y-800°C-3h, which was directly calculated from the XRD data, was used as a reference. The lattice parameter value of the 01Er-800°C-3h sample was used to estimate the lattice parameter value of un-doped Er_2O_3 crystals assuming that full solid solution was achieved in the 1at% Er doped sample. Raman spectrum was taken at room temperature using 632.81 nm laser so as to evidence the existence of Er

Table 1. Sample designations and synthesis parameters

Designation	Dopant rate / at%	Calcination temperature / °C	Calcination time / h
05Er	5	—	—
Y-800°C-3h	0	800	3
01Er-800°C-3h	1	800	3
05Er-800°C-3h	5	800	3
10Er-800°C-3h	10	800	3
20Er-800°C-3h	20	800	3
05Er-1100°C-3h	5	1100	3

dopant element. Morphology examinations were performed with scanning electron microscopy (SEM) by TESCAM MAIA3 XMU. In order to validate the nanostructure of the NPs, transmission electron microscopy (TEM) was used with an accelerating voltage of 200 kV by FEI TALOS F200S. X-ray photoelectron spectroscopy (XPS) analysis was performed to verify that the Er ions enter into Y_2O_3 host lattice. The radioluminescence (RL) studies were examined under a Cu K_α X-ray radiation (λ = 0.154 nm) source with 50 kV and 10 mA beam current, and radioluminescence emission spectra were recorded in the range of 300–800 nm.

3. Results and discussion

3.1. DTA–TG analysis

The results of the DTA–TG analysis for 5at% Er doped Y_2O_3 sample is given in Fig. 1. The broad endothermic peak around 110°C indicates the removal of water molecules. On the other hand, the sharp exothermic peak at about 380°C is due to the removal of organic compounds and crystallization of Y_2O_3 phase. There was not any other peak observed above 400°C. The weight loss finished at about 750°C. According to the thermal analysis, the samples were calcined at the temperature above 750°C which was 800°C.

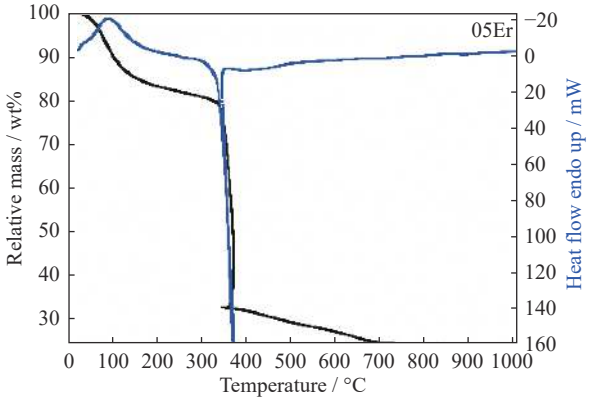

Fig. 1. DTA–TG analysis of 05Er coded sample.

3.2. XRD analysis and microstructural parameters

The XRD patterns of the calcined samples are given in Fig. 2. All samples had body-centered cubic Y_2O_3 crystal structure (space group Ia-3, JCPDS card No. 00-025-1200). Increasing dopant rate shifted the diffraction peaks to the higher angles (inset in Fig. 2) indicating shrinkage of the crystal. When the smaller Er^{3+} ions (0.0881 nm) substituted for relatively larger host Y^{3+} (0.0892 nm) [7,40] ions, the crystal of the Y_2O_3 host structure became smaller and the diffraction peaks shifted to the higher angles.

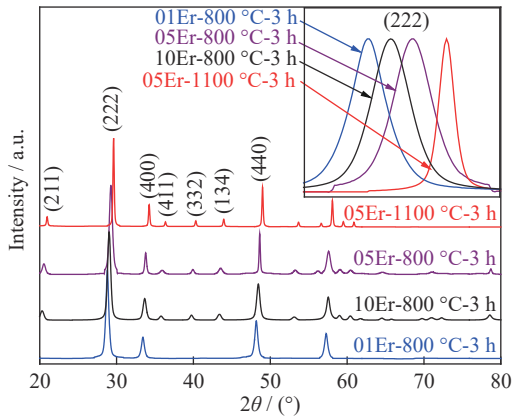

Fig. 2. XRD patterns of Y_2O_3:Er^{3+} phosphors. Inset shows the magnified (222) diffraction peaks.

The lattice parameters and crystallite sizes/lattice strains of Y_2O_3:Er^{3+} phosphors were calculated from the XRD patterns (Table 2) by W-H and C-W methods, respectively.

The calculated lattice parameter values confirmed that Er^{3+} ions incorporated into the Y_2O_3 structure. As an example, the C-W plots of 01Er-800°C-3h and 05Er-800°C-3h samples are given in Fig. 3. The lattice parameter values of these samples were 1.0612 nm and 1.0606 nm with the regression coefficient values (R^2) of 89.3% and 99.9%, respectively. In order to determine the optimum solubility of Er^{3+} ions in Y_2O_3 host, "Vegard's law" was used. When the lattice parameter values of un-doped (Y-800°C-3h, 1.0614 nm) and 1at% Er^{3+} doped (01Er-800°C-3h, 1.0612 nm) were considered, the lattice parameter of un-doped Er_2O_3 crystal was estimated to be 1.0414 nm which is close to the 5 h calcined sample at 800°C (1.0548 nm) in the literature [7,41]. By using this value, the dopant rate was found to be 4at% when the lattice parameter of 5at% Er samples was used, which is the lowest lattice parameter obtained among the 800°C calcined samples. Further increment of Er^{3+} ions in the precursor solution (10at% and 20at%), decreased the dopant rate to 3at%,

Table 2. Lattice parameter, crystallite size, lattice strain, and dislocation density values of Y_2O_3:Er^{3+} phosphors

Designation	Lattice parameter, a / nm	Crystallite size, D / nm	Lattice strain, ε	Dislocation density, δ / nm^{-2}
01Er-800°C-3h	1.0612	20	-9.589×10^{-5}	0.00250
10Er-800°C-3h	1.0608	17	-6.765×10^{-4}	0.00346
20Er-800°C-3h	1.0608	18	-2.389×10^{-4}	0.00308
05Er-800°C-3h	1.0606	15	-7.519×10^{-4}	0.00444
05Er-1100°C-3h	1.0601	44	-2.894×10^{-4}	0.00051

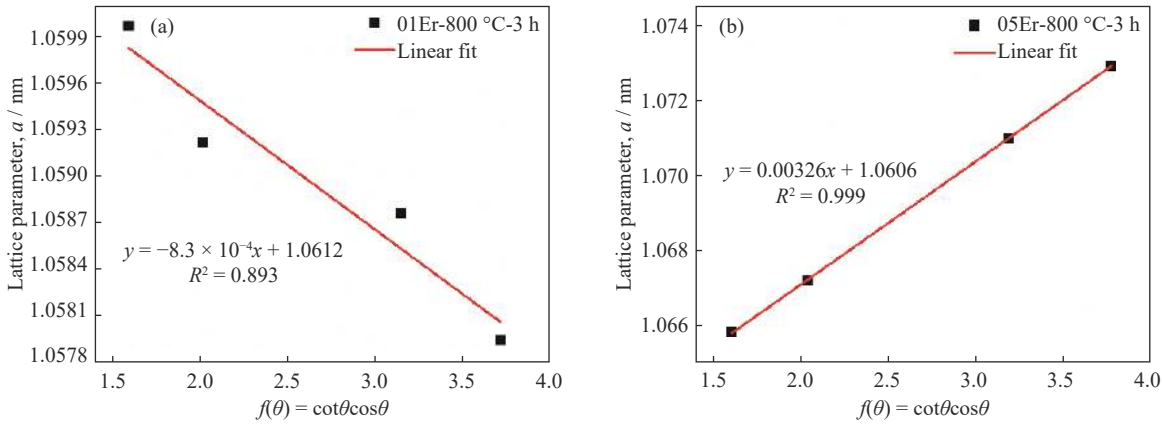

Fig. 3. C-W plots of (a) 01Er-800°C-3h and (b) 05Er-800°C-3h coded samples.

according to the Vegard's law. This analysis suggested that the maximum Er^{3+} solubility was 4at% in our experiments for the 05Er-800°C-3h sample.

On the other hand, according to the W-H graphs (Fig. 4), the crystallite size values of 01Er-800°C-3h and 05Er-800°C-3h samples were 20 nm and 15 nm with the regression coefficient values (R^2) of 92.3% and 97.9%, respectively. It was observed that dopant rate made the crystallite size of the phosphors smaller, indicating a positive correlation between crystallite size and lattice parameter (Fig. 5(a)).

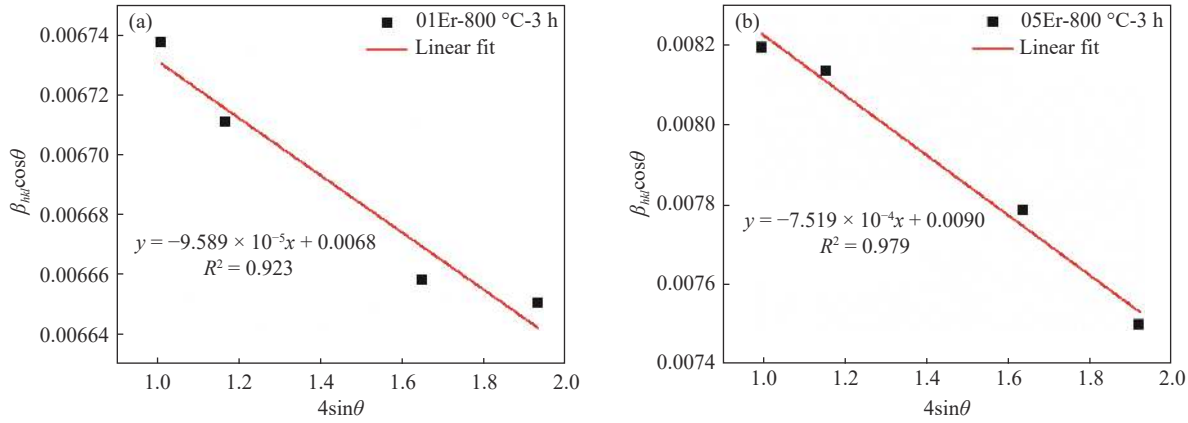

Fig. 4. W-H plots of (a) 01Er-800°C-3h and (b) 05Er-800°C-3h coded samples.

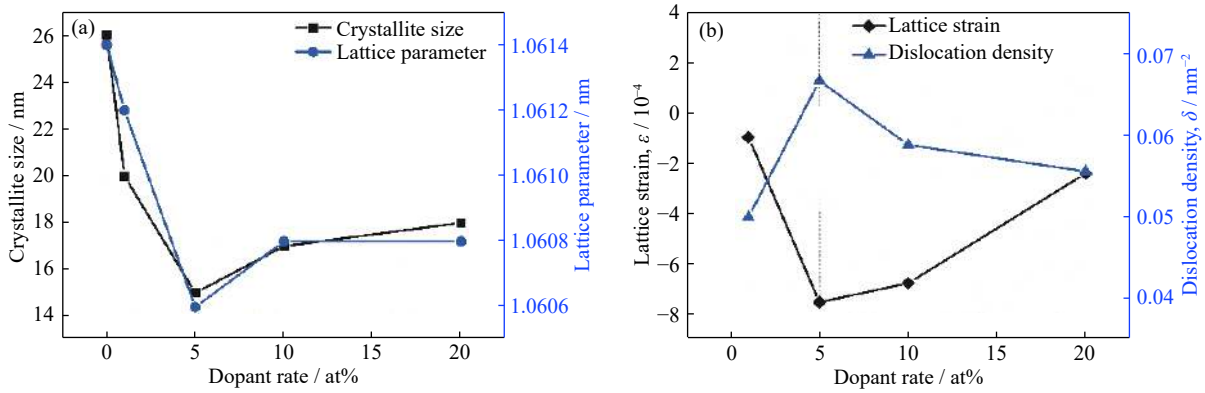

Fig. 5. (a) Crystallite size and lattice parameter and (b) lattice strain and dislocation density as a function of dopant rate.

If the calculated lattice strain and dislocation density values are considered (Fig. 5(b)), this trend could be attributed to the increasing crystal imperfection with the doping, which in return limited the growth of the crystallite. Therefore, smaller crystallites were obtained with increasing dopant rate. Maximum lattice strain and dislocation density was observed for the 05Er-800°C-3h sample, which was consistent with the XRD peak shifts and Vegard's analyses. Further addition of

Er^{3+} ions into the solution (10at% and 20at%) increased the crystallite size (Fig. 5(a)) and decreased the lattice strain, in other words, decreased the dislocation density (Fig. 5(b)). These results suggest that further addition of Er ions into the solution beyond 5at%, affects Er incorporation into the Y_2O_3 lattice negatively, thus based on the above explanations, the crystallite sizes were increased.

The calcination temperature had an effect on the peak shift similar to the Er substitute. When the calcination temperature was increased to 1100°C for the 5at% Er doped sample, the XRD peaks were shifted to the higher diffraction angles more notably (inset in Fig. 2). The lattice parameter and crystallite size of the 05-1100°C-3h sample were calculated to be 1.0601 nm and 44 nm, respectively. This result suggests that Er^{3+} incorporation into the Y_2O_3 lattice was induced with increased crystallite size which can be attributed to reduced dislocation density (Table 2).

3.3. TEM and SEM analyses

The TEM image of 05-800°C-3h sample reveals the presence of aggregated nearly spherical NPs (Fig. 6(a)). The aggregated NP sizes were found to be ranging from 10 to 20 nm which supports the average CS calculated by W-H analyses (15 nm). The high resolution TEM (HRTEM) image (Fig. 6(c)) reveals a highly crystalline structure. The lattice fringe (*d*) was determined from HRTEM image and indexed to $d_{(400)}$ = 0.265 nm of the cubic Y_2O_3 phase. Utilizing the *d* value, the lattice parameter calculated from (400) diffraction peak and found to be around 1.06 nm. The scanning electron micrographs of 05-1100°C-3h sample are given in Figs. 6(d)–6(e). Partly sintered porous ceramic structure was clearly observed in Fig. 6(d). The neck formation between the particles was visible, indicating that sintering mechanisms were activated due to increased calcination temperature (Fig. 6(e)).

3.4. X-ray photoelectron spectroscopy (XPS) analysis

Wide scan XPS spectrum of the 05Er-1100°C-3h sample is given in Fig. 7. In order to compensate the surface charge effects on the insulating sample, all binding energies were corrected with C 1s reference peak at 284.80 eV. The peak positions are listed in Table 3.

The signals at 169.41 and 179.81 eV binding energy were of Er 4d and Er $4d_{3/2}$ level, respectively. Thus, the incorporation of Er^{3+} ion into the Y_2O_3 host structure was confirmed by XPS analysis. Except for the elements given in the table, any impurities (particularly Eu) were not found in the sample.

3.5. Single photon counters results

Single photon counters studies of the phosphor powders were performed with Cu K_α X-ray radiation exposure with 50 kV and 10 mA beam current to determine the optimum dopant rate. Emission intensity–bin number plots are given in Fig. 8. It was observed that 1at% Er doped sample had the lowest emission counts whereas 5at% Er doped sample exhibited the highest emission intensity. The emission intensity values decreased for the 10at% and 20at% Er samples. In fact, 20at% Er sample exhibited slightly lower emission than that of the 10at% Er sample which suggests that the observed dopant rate of the 10at% Er sample is probably higher than the 20at% Er sample. These results clearly showed that 5at% Er doped sample had the highest Er incorporation, as also demonstrated by the XRD, C-W and Vegard's analyses. In

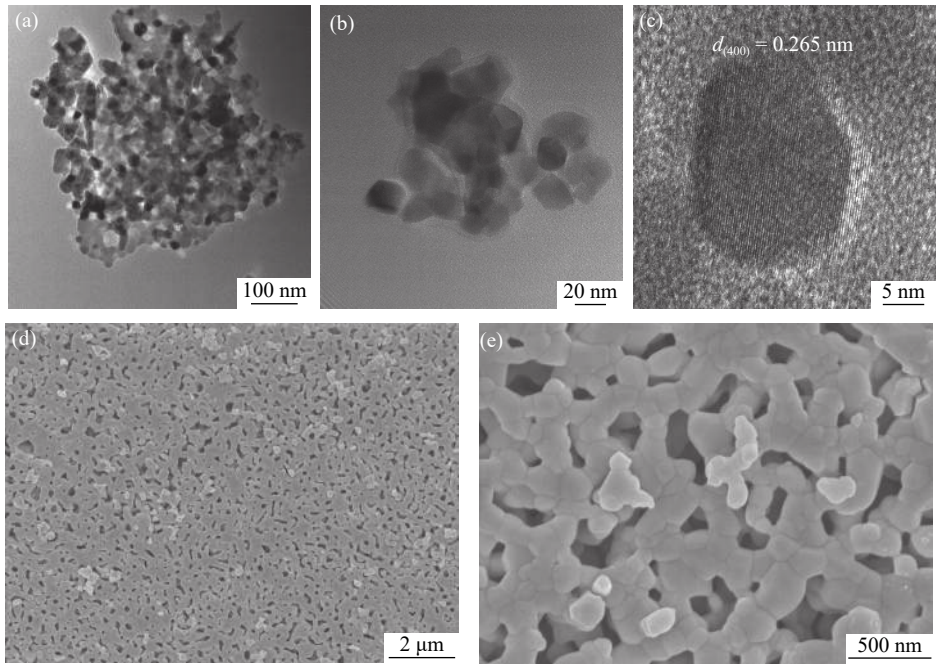

Fig. 6. (a–c) TEM images of 05-800°C-3h coded sample and (d, e) SEM images of 05-1100°C-3h coded sample.

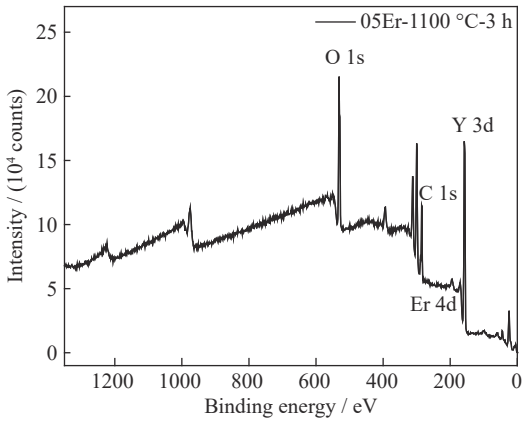

Fig. 7. XPS survey spectrum of 05Er-1100°C-3h coded sample..

Table 3. Peak positions of elements

Element	Peak position / eV	Corrected peak position / eV
C 1s	285.42	284.80
O 1s	532.33	531.71
Y 3d	157.22	156.60
Er 4d	170.03	169.41
Er $4d_{3/2}$	180.43	179.81

consideration of the results, the 5at% doped Y_2O_3 sample having highest sensitivity to the X-ray radiation was further studied.

3.6. Radioluminescence (RL) measurements

RL measurements of 05Er-800°C-3h and 05Er-1100°C-3h samples were given in Fig. 9. The high energy X-ray excitation resulted in emissions from the sample within a high wavelength range. It was seen that emission peaks were in the range of 510–575 nm and 645–690 nm belonging to $^2H_{11/2}$, $^4S_{3/2}$–$^4I_{15/2}$ (green emission) and $^4F_{9/2}$–$^4I_{15/2}$ (red emission) transitions of Er ion, respectively [37,42]. The emission peaks within 515–534 nm and 645–690 nm appeared for the sample calcined at higher calcination temperature (1100°C). Moreover, the emission from this sample became more intense within the wavelength range of 535–575 nm, as observed in Avram *et al.*'s work [37]. Also, there is no change observed in the emission intensity of the peaks between 578 and 640 nm with increased calcination temperature. However, in contrast to Avram *et al.* [37], we observed a strong peak at 611 nm in the emission band between 578–640 nm, not affected by increased crystallinity, supporting the idea of the emission band originated from the Y_2O_3 host or some energy levels of Er ion [42–43]. Benefiting the color space values, the color temperature values of 05Er-800°C-3h and 05Er-1100°C-3h samples were determined to be 2882 K and 3506 K, respectively [1,44]. It was observed that the emission color shifted from red to green as the calcination temperature increasing. Together with the crystallite size/dislocation density relation explained in the Section 3.2, it could be concluded that the amount of Er^{3+} ions on the defective sites such as surfaces, crystallite boundaries, O^{2-} vacant sites etc., was reduced with increased crystallite size (15 to 44 nm), and this promoted Er^{3+} incorporation into the ideal Y^{3+} sites (C_2, C_{3i}). Thus, defect induced luminescence quenching was minimized in the 05Er-1100°C-3h sample and emission intensities from Er centers were increased.

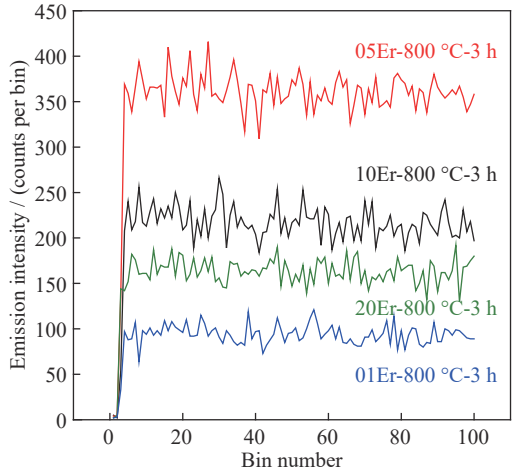

Fig. 8. Emission intensity–bin number plots of Y_2O_3:Er^{3+} nanophosphors calcined at 800°C for 3 h.

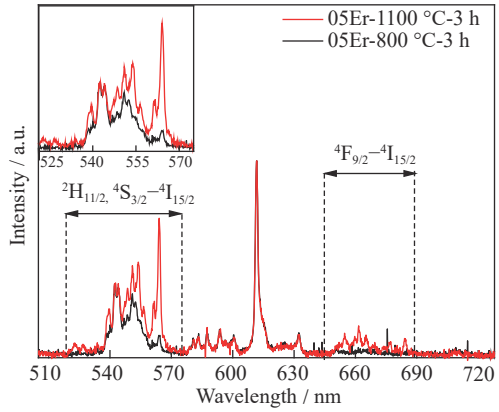

Fig. 9. RL spectra of 05Er-800°C-3h and 05Er-1100°C-3h coded samples. Inset shows magnified $^2H_{11/2}$, $^4S_{3/2}$–$^4I_{15/2}$ transition peaks (green emission).

4. Conclusion

The erbium-doped yttria nanophosphors were produced by means of facile sol–gel method. The samples had body-centered Y_2O_3 cubic crystal structure (space group Ia-3). The peak shifts in the XRD patterns and the Er 4d XPS peak verified the incorporation of Er^{3+} to the Y_2O_3 host structure. By applying the Vegard's law, the optimum solubility of Er^{3+} ions in the Y_2O_3 lattice was found to be 4at%. According to

the W-H analyses, the dopant rate was found to decrease the CS of the phosphors, which were between 15 and 20 nm for the samples calcined at 800°C for 3 h. Agglomerated nearly spherical nanoparticle structure was revealed by HRTEM analysis which confirms the average CS values obtained via W-H analysis. On the other hand, increasing calcination temperature (1100°C) enlarged the crystallites (44 nm). Due to the increased calcination temperature, the sintering mechanisms were activated and the neck formation between the particles was clearly seen in the SEM analysis. According to the RL emission experiments, the lowest emission was obtained for the 1at% Er doped sample, whereas 5at% Er doped Y_2O_3 sample exhibited the highest RL emission intensity, which confirms the maximum solubility was obtained for this sample. The RL emission peaks within 510–575 nm corresponding to the $^2H_{11/2}$, $^4S_{3/2}$–$^4I_{15/2}$ (green emission) transitions and within 645–690 nm corresponding to the $^4F_{9/2}$–$^4I_{15/2}$ (red emission) transitions from Er centers were observed. Additionally, there were peaks between 578–640 nm emission band (peaking at 611 nm) which were possibly originated from the host Y_2O_3 or Er ion. The color temperatures of 05Er-800°C-3h and 05Er-1100°C-3h samples were found to be 2882 K and 3506 K, respectively. The color of the emission shifted from red to green with increasing crystallite size which was due to the incorporation of Er^{3+} ions into the ideal Y^{3+} sites with increased crystalize size. These results show that 5at% Er-doped Y_2O_3 phosphors are promising materials for scintillator applications.

Acknowledgements

This work was financially supported by the Teaching Staff Training Program (OYP) Project, Turkey. The authors appreciate Berk Alkan for his valuable help in radioluminescence measurements.

References

[1] F. Unal, F. Kaya, and K. Kazmanli, Effects of dopant rate and calcination parameters on photoluminescence emission of Y_2O_3:Eu^{3+} phosphors: A statistical approach, *Ceram. Int.*, 45(2019), No. 14, p. 17818.

[2] T. Minami, Y. Kobayashi, T. Miyata, and M. Yamazaki, High-luminance thin-film electroluminescent devices using Y_2O_3:Mn phosphor, *Thin Solid Films*, 443(2003), No. 1-2, p. 91.

[3] R.H. Krishna, B.M. Nagabhushana, H. Nagabhushana, N.S. Murthy, S.C. Sharma, C. Shivakumara, and R.P.S. Chakradhar, Effect of calcination temperature on structural. photoluminescence.and thermoluminescence properties of Y_2O_3:Eu^{3+} nanophosphor, *J. Phys. Chem. C*, 117(2013), No. 4, p. 1915.

[4] L.G. Jacobsohn, B.L. Bennett, R.E. Muenchausen, J.F. Smith, and D.W. Cooke, Optical and structural characterization of nanostructured Y_2O_3:Tb, [in] *Proc. SPIE 6321, Nanophotonic Materials III*, San Diego, 2006.

[5] R. Pflieger, L. Gravier, G. Guillot, M. Ashokkumar, and S.I. Nikitenko, Inverse effects of the gas feed positioning on sonochemistry and sonoluminescence, *Ultrason. Sonochem.*, 46(2018), p. 10.

[6] S.S. Pitale, V. Kumar, I.M. Nagpure, O.M. Ntwaeaborwa, E. Coetsee, and H.C. Swart, Cathodoluminescent properties and surface characterization of bluish-white $LiAl_5O_8$:Tb phosphor, *J. Appl. Phys.*, 109(2011), No. 1, art. No. 013105.

[7] F. Unal and K. Kazmanli, Production of un-doped and Er-doped Y_2O_3 thin films by electron beam evaporation method, *Powder Metall. Met. Ceram.*, 58(2019), No. 3-4, p. 204.

[8] X. Zhang, H.L. Zhao, S. Gao, and Q.F. Zeng, First-principles study of electronic structure and optical properties of Er:Lu_2O_3, *J. Rare Earths*, 39(2021), No. 4, p. 453.

[9] D.A. Permin, S.S. Balabanov, I.L. Snetkov, O.V. Palashov, A.V. Novikova, O.N. Klyusik, and I.V. Ladenkov, Hot pressing of Yb:Sc_2O_3 laser ceramics with LiF sintering aid, *Opt. Mater.*, 100(2020), art. No. 109701.

[10] B.P. Gangwar, S. Irusta, and S. Sharma, Physicochemical and optical properties of one-pot combustion synthesized Pr doped La_2O_3/$La(OH)_3$, *J. Lumin.*, 219(2020), art. No. 116893.

[11] Y.Z. Wang, Z.C. Wen, W.G. Ye, Z. Feng, C. Zhao, C.D. Zuo, Y.B. Li, Z.Q. Cao, Z.J. Cao, C.Y. Ma, and Y.G. Cao, Enhanced green up-conversion luminescence in In_2O_3:Yb^{3+}/Er^{3+} by tri-doping Zn^{2+}, *J. Lumin.*, 221(2020), art. No. 117029.

[12] A. Ćirić and S. Stojadinović, Photoluminescence of Gd_2O_3 and Gd_2O_3:Ln^{3+} (Ln = Eu, Er, Ho) formed by plasma electrolytic oxidation of pure gadolinium substrate, *Opt. Mater*, 99(2020), art. No. 109546.

[13] Y.Z. Li, T. Cai, L.X. Yang, S.T. Guo, D. Peng, X.F. Zhao, and Y.Z. Liu, Effect of oxygen partial pressure on the phosphorescence of different lanthanide ion (Ln^{3+})-doped yttria-stabilised zirconia, *Sens. Actuators B*, 308(2020), art. No. 127666.

[14] L.X. Yang, D. Peng, X. Shan, F.W. Guo, Y.Z. Liu, X.F. Zhao, and P. Xiao, "Oxygen quenching" in Eu-based thermographic phosphors: Mechanism and potential application in oxygen/pressure sensing, *Sens. Actuators B*, 254(2018), p. 578.

[15] T.T. Van, J.R. Bargar, and J.P. Chang, Er coordination in Y_2O_3 thin films studied by extended x-ray absorption fine structure, *J. Appl. Phys.*, 100(2006), No. 2, art. No. 023115.

[16] H. Guo and Y.M. Qiao, Preparation, characterization, and strong upconversion of monodisperse Y_2O_3:Er^{3+},Yb^{3+} microspheres, *Opt. Mater.*, 31(2009), No. 4, p. 583.

[17] V.K. Rai, A. Pandey, and R. Dey, Photoluminescence study of Y_2O_3:Er^{3+}–Eu^{3+}–Yb^{3+} phosphor for lighting and sensing applications, *J. Appl. Phys.*, 113(2013), No. 8, art. No. 083104.

[18] Q.P. Lu, Y.B. Hou, A.W. Tang, X.J. Liu, and F. Teng, Synthesis of porous Y_2O_3:Er plates with enhanced upconversion luminescence properties, *Mater. Lett.*, 99(2013), p. 115.

[19] T. Hirai, T. Orikoshi, and I. Komasawa, Preparation of Y_2O_3:Yb,Er infrared-to-visible conversion phosphor fine particles using an emulsion liquid membrane system, *Chem. Mater.*, 14(2002), No. 8, p. 3576.

[20] T. Nunokawa, O. Odawara, and H. Wada, Optical properties of highly crystalline Y_2O_3:Er,Yb nanoparticles prepared by laser ablation in water, *Mater. Res. Express*, 1(2014), No. 3, art. No. 035043.

[21] V. Lojpur, L. Mancic, P. Vulic, M.D. Dramicanin, M.E. Rabanal, and O. Milosevic, Structural, morphological and up-converting luminescence characteristics of nanocrystalline Y_2O_3:Yb/Er powders obtained via spray pyrolysis, *Ceram. Int.*, 40(2014), No. 2, p. 3089.

[22] J.I. Eldridge, Luminescence decay-based Y_2O_3:Er phosphor thermometry: Temperature sensitivity governed by multiphon-

on emission with an effective phonon energy transition, *J. Lumin.*, 214(2019), art. No. 116535.

[23] C.C. Mi, J.P. Zhang, H.Y. Gao, X.L. Wu, M. Wang, Y.F. Wu, Y.Q. Di, Z.R. Xu, C.B. Mao, and S.K. Xu, Multifunctional nanocomposites of superparamagnetic (Fe_3O_4) and NIR-responsive rare earth-doped up-conversion fluorescent ($NaYF_4$:Yb,Er) nanoparticles and their applications in biolabeling and fluorescent imaging of cancer cells, *Nanoscale*, 2(2010), No. 7, p. 1141.

[24] F.L. Meng, Y. Luo, Y.L. Zhou, J.W. Zhang, Y.Z. Zheng, G.Z. Cao, and X. Tao, Integrated plasmonic and upconversion star-like Y_2O_3:Er/Au@TiO_2 composite for enhanced photon harvesting in dye-sensitized solar cells, *J. Power Sources*, 316(2016), p. 207.

[25] R. Dey, A. Pandey, and V.K. Rai, Er^{3+}–Yb^{3+} and Eu^{3+}–Er^{3+}–Yb^{3+} codoped Y_2O_3 phosphors as optical heater, *Sens. Actuators B*, 190(2014), p. 512.

[26] D.L. Yin, J. Wang, Y. Wang, P. Liu, J. Ma, X.D. Xu, D.Y. Shen, Z.L. Dong, L.B. Kong, and D.Y. Tang, Fabrication of Er:Y_2O_3 transparent ceramics for 2.7 μm mid-infrared solid-state lasers, *J. Eur. Ceram. Soc.*, 40(2020), No. 2, p. 444.

[27] T. Yanagida, Study of rare-earth-doped scintillators, *Opt. Mater.*, 35(2013), No. 11, p. 1987.

[28] K. Rubešová, T. Thoř, V. Jakeš, D. Mikolášová, J. Maixner, O. Jankovský, J. Cajzl, L. Nádherný, Lanthanide-doped Y_2O_3 – The photoluminescent and radioluminescent properties of sol–gel prepared samples, *Ceram. Silik.*, 62(2018), No. 4, p. 411.

[29] Y. Fujimoto, T. Yanagida, Y. Yokota, A. Ikesue, and A. Yoshikawa, Evaluation of characterization of rare-earth doped sesquioxide ceramic scintillators, *Opt. Mater.*, 34(2011), No. 2, p. 448.

[30] I. Kandarakis, D. Cavouras, D. Nikolopoulos, P. Liaparinos, A. Episkopakis, K. Kourkoutas, N. Kalivas, N. Dimitropoulos, I. Sianoudis, C. Nomicos, and G. Panayiotakis, Modelling angular distribution of light emission in granular scintillators used in X-ray imaging detectors, [in] A. Méndez-Vilas, ed., *Proceedings of the First International Meeting on Applied Physics (APHYS-2003)*, Badajoz, 2003, p. 909.

[31] N. Kumamoto, D. Nakauchi, T. Kato, G. Okada, N. Kawaguchi, and T. Yanagida, Photoluminescence, scintillation and thermally-stimulated luminescence properties of Tb-doped 12CaO•7Al_2O_3 single crystals grown by FZ method, *J. Rare Earths*, 35(2017), No. 10, p. 957.

[32] B.K. Cha, S.J. Lee, P. Muralidharan, J.Y. Kim, D.K. Kim, D.H. Lee, J.I. Yun, and G. Cho, Synthesis and scintillation properties of nano Gd_2O_3(Eu) scintillator for high resolution X-ray imaging applications, *Nucl. Instrum. Methods Phys. Res. Sect. A*, 619(2010), No. 1-3, p. 174.

[33] K. Kamada, K. Hishinuma, S. Kurosawa, A. Yamaji, Y. Shoji, J. Pejchal, Y. Ohashi, Y. Yokota, and A. Yoshikawa, Growth and luminescence properties of Eu-doped HfO_2/α-Al_2O_3 eutectic scintillator, *J. Rare Earths*, 34(2016), No. 8, p. 796.

[34] S. Fukushima, T. Furukawa, H. Niioka, M. Ichimiya, T. Sannomiya, J. Miyake, M. Ashida, T. Araki, and M. Hashimoto, Synthesis of Y_2O_3 nanophosphors by homogeneous precipitation method using excessive urea for cathodoluminescence and upconversion luminescence bioimaging, *Opt. Mater. Express*, 6(2016), No. 3, p. 831.

[35] Y.B. Mao, X. Guo, T. Tran, K.L. Wang, C.K. Shih, and J.P. Chang, Luminescent properties of ensemble and individual erbium-doped yttrium oxide nanotubes, *J. Appl. Phys.*, 105(2009), No. 9, art. No. 094329.

[36] D. den Engelsen, G.R. Fern, T.G. Ireland, and J. Silver, Cathodoluminescence of Y_2O_3:Ln^{3+} (Ln = Tb, Er and Tm) and Y_2O_3:Bi^{3+} nanocrystalline particles at 200 keV, *RSC Adv.*, 8(2018), No. 1, p. 396.

[37] D. Avram, B. Cojocaru, I. Tiseanu, M. Florea, and C. Tiseanu, Down-/up-conversion emission enhancement by Li addition : Improved crystallization or local structure distortion?, *J. Phys. Chem. C*, 121(2017), No. 26, p. 14274.

[38] A.S. Hassanien, A.A. Akl, and A.H. Sáaedi, Synthesis, crystallography, microstructure, crystal defects, and morphology of $Bi_xZn_{1-x}O$ nanoparticles prepared by sol–gel technique, *CrystEngComm*, 20(2018), No. 12, p. 1716.

[39] Z.C. Cordero and C.A. Schuh, Phase strength effects on chemical mixing in extensively deformed alloys, *Acta Mater.*, 82(2015), p. 123.

[40] R.V. Perrella, D.P. dos Santos, G.Y. Poirier, M.S. Góes, S.J.L. Ribeiro, M.A. Schiavon, and J.L. Ferrari, Er^{3+}-doped Y_2O_3 obtained by polymeric precursor: Synthesis, structure and upconversion emission properties, *J. Lumin.*, 149(2014), p. 333.

[41] W. Zhong, H.X. Dai, C.F. Ng, and C.T. Au, A comparison of nanoscale and large-size $BaCl_2$-modified Er_2O_3 catalysts for the selective oxidation of ethane to ethylene, *Appl. Catal. A*, 203(2000), No. 2, p. 239.

[42] S. Agrawal and V. Dubey, Down conversion luminescence behavior of Er and Yb doped Y_2O_3 phosphor, *J. Radiat. Res. Appl. Sci.*, 7(2014), No. 4, p. 601.

[43] H. Huang, X.H. Sun, S.D. Wang, Y. Liu, X.R. Li, J.L. Liu, Z.H. Kang, and S.T. Lee, Strong red emission of pure Y_2O_3 nanoparticles from oxygen related defects, *Dalton Trans.*, 40(2011), No. 43, p. 11362.

[44] The International Commission on Illumination (CIE), *Fundamental Chromaticity Diagram with Physiological Axes. Part 1*, Technical Report 170-1, CIE Central Bureau, Vienna, 2006.